IEEE Photonics Journal
An IEEE Photonics Society Publication

Open Access

Dual Mach–Zehnder Interferometer Based on Side-Hole Fiber for High-Sensitivity Refractive Index Sensing

Volume 11, Number 6, December 2019

Jie Hu
Liyang Shao, *Senior Member, IEEE*
Guoqiang Gu
Xuming Zhang
Yanjun Liu
Xuefeng Song
Zhangqi Song
Jiansong Feng
Ryszard Buczyński
Mateusz Śmietana
Taihong Wang
Tingting Lang

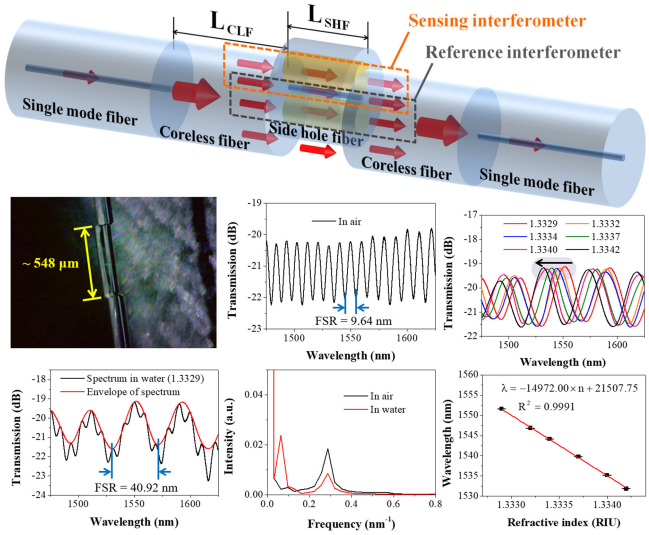

DOI: 10.1109/JPHOT.2019.2948087

Dual Mach–Zehnder Interferometer Based on Side-Hole Fiber for High-Sensitivity Refractive Index Sensing

Jie Hu [1,2] Liyang Shao [1] *Senior Member, IEEE*, Guoqiang Gu [1] Xuming Zhang [3] Yanjun Liu [1] Xuefeng Song,[4] Zhangqi Song,[4] Jiansong Feng,[1] Ryszard Buczyński,[5] Mateusz Śmietana [6] Taihong Wang,[1] and Tingting Lang [2]

[1]Department of Electrical and Electronic Engineering, Southern University of Science and Technology, Shenzhen 518055, China
[2]Institute of Optoelectronic Technology, China Jiliang University, Hangzhou 310018, China
[3]Department of Applied Physics, Hong Kong Polytechnic University, Hong Kong
[4]School of Innovation and Entrepreneurship, Southern University of Science and Technology, Shenzhen 518055, China
[5]Faculty of Physics, University of Warsaw, Warsaw 02-093, Poland, and also with the Institute of Electronic Materials Technology, Warsaw 01-919, Poland
[6]Institute of Microelectronics and Optoelectronics, Warsaw University of Technology, Warsaw 00-662, Poland

DOI:10.1109/JPHOT.2019.2948087

Manuscript received May 23, 2019; revised August 28, 2019; accepted October 15, 2019. Date of publication October 17, 2019; date of current version December 13, 2019. This work was supported in part by the National Natural Science Foundation of China under Grant 61475128 and Grant 61875251 and in part by the National Science Centre (NCN) of Poland as a part of 2018/29/B/ST7/02552 project. Corresponding authors: Liyang Shao; Tingting Lang (e-mail: shaoly@sustech.edu.cn; langtingting@cjlu.edu.cn).

Abstract: A unique type of refractive index (RI) sensor is proposed using a dual Mach-Zehnder interferometer (MZI) structure based on side-hole fibers (SHFs). The MZI structure contains two single-mode fibers (SMFs), two coreless fiber (CLF) sections and an SHF section, which are spliced together in the order of SMF-CLF-SHF-CLF-SMF. The SMFs and the CLFs enable light lead in/out and beam splitting/combining, respectively. As a special feature of the structure, one hole of SHF is exposed for liquid filling and to form two MZIs as well. Three types of sensors are fabricated, namely S1, S2 and S3. Numerical simulation and experimental studies have been conducted to characterize the sensing performance. The RI sensitivity of the S1 using the $\sim$550 μm long SHF section reaches 14,000 nm/RIU. When a shorter SHF section is used in S2, the detectable RI range is broadened due to larger FSR. When the closed hole of SHF in S3 is filled with liquid to introduce the Vernier effect, the sensitivity can be further enhanced to over 44,000 nm/RIU (i.e., Refractive Index Unit), which corresponds to the detection limit at the level of 1.0×10^{-5} RIU. This sensor design is original and easy to package, which gives it potential for label-free biochemical analyses.

Index Terms: Optical fiber sensor, refractive index sensing, side-hole fiber, Mach-Zehnder interferometer, Vernier effect.

1. Introduction

Refractive index (RI) sensing of liquids is essential for chemical and biological experiments because the RI directly reflects the composition changes of liquids. In contrast to the widely-used prism-based

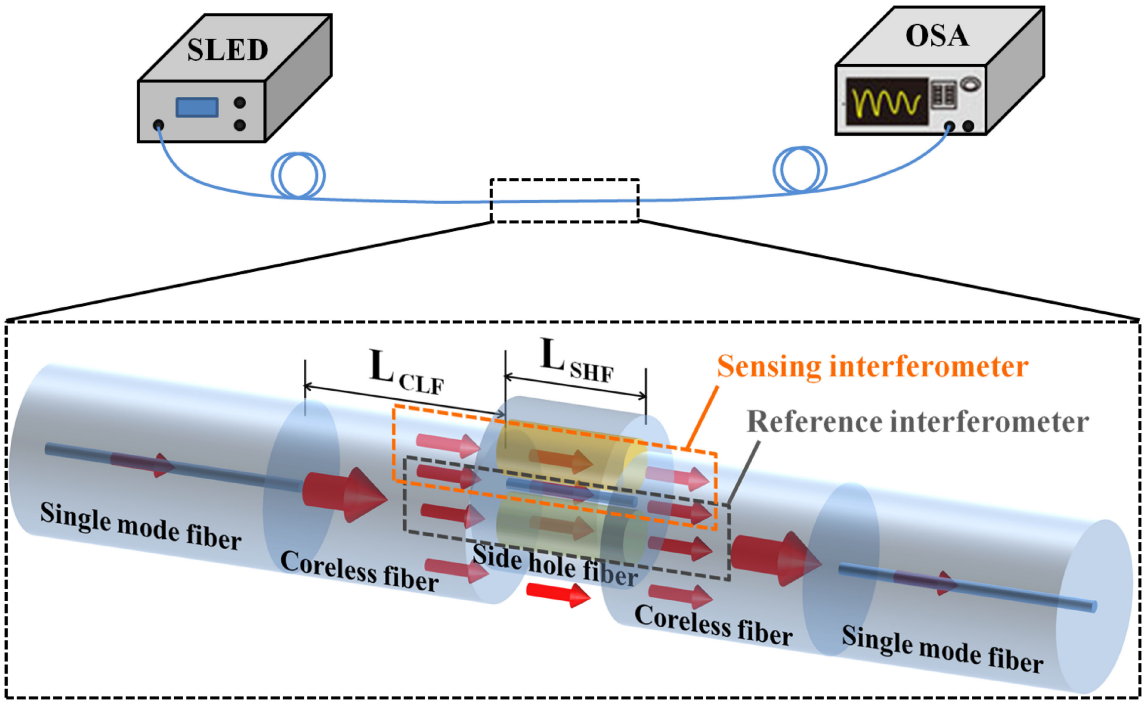

Fig. 1. Schematic diagram of the dual Mach-Zehnder interferometer based on the side-hole fiber.

refractometers, the RI sensors based on optical fibers offer many advantages, such as immunity to electromagnetic interference, high sensitivity, and low cost, and when biological sensing is considered – easy sample disposal. Various optical fiber RI sensors have been reported based on fiber Bragg gating (FBG) [1], [2], long-period grating (LPG) [3], [4], tapered fiber [5]–[8], and Fabry-Perot interferometer (FPI) [9], [10]. Among them, fiber-based Mach-Zehnder (MZI) [11]–[14] and Michelson [15], [16] interferometers are extensively studied for RI sensing. When the MZI is formed by using a microcavity fabricated in an optical fiber [17], exceptional sensitivity can be obtained due to the tight optical confinement of the microcavity, for example, a recent study showed a sensitivity of over 10,000 nm/RIU (i.e., Refractive Index Unit) [18].

Although various structures and mechanisms have been proposed, the area of interaction between the optical field in the fiber and the liquid is still very limited. Microstructured optical fibers (MOFs) [19]–[21], especially hollow-core photonic crystal fibers [22], [23], offer a perfect platform for flowing fluids and guide light in the same path, which would significantly enhance the direct/indirect interactions between the light and the liquid. Moreover, the air hole region in an MOF acts as a small-volume chemical reactor and is very promising for chemical sensing and photochemistry.

As a special type of MOF, side-hole fiber (SHF) contains two large air holes on both sides of the central core and will be used in this paper. Here, we will construct an RI sensor using a laterally offset section of SHF to form two Mach-Zehnder interferometers. The structure will be analyzed theoretically and numerically, and its performance will be examined experimentally.

2. Design and Experimental Details

The schematic representation of the proposed sensor is shown in Fig. 1. It contains a laterally-offset section of SHF between two sections of coreless fibers (CLF). The SHF (Yangtze Optical Electronic Co., Wuhan, China) has two large air holes beside the core. The diameters of the core, air holes and cladding are 9 μm, 37 μm and 114 μm, respectively. Two holes are symmetrically distributed on both sides of the core with a gap (edge distance) of 12 μm. One of the air holes is exposed

to external medium due to the lateral offset. The CLF is made of fused silica and has a diameter of 125 μm. The core diameter and the cladding diameter of the single mode fiber (SMF, model SMF-28e, Corning) are 8.2 μm and 125 μm, respectively. The SMFs at both the CLF ends act as the input and output fibers that are connected to a broadband light source (HOYATEK, HY-SLED-1550-10-90-8-FC/APC-T) and an optical spectrum analyzer (YOKOGAWA AQ6370D), respectively. The wavelength range of interrogation is 1450–1650 nm.

As indicated by the arrows in Fig. 1, the light from the input SMF is transmitted into the section of CLF, which acts as a beam splitter, and then, it is transmitted into both the air holes and the silica part of the SHF. Next, the beams are combined in the second CLF and finally transmitted into the lead-out SMF. Here, the length of the CLF (L_{CLF}) was chosen to be almost 1 mm to ensure that there is sufficient light coupled into the air holes of the SHF without exciting obvious multimode interference in the CLF section. The light beams interfere with one another and can be treated as a combination of two MZIs. One MZI acts as the sensing element and transmits the light through both the silica part and the exposed hole, which can be filled with a sample. Similarly, the other MZI works as the reference element. The difference is that the hole is closed and immune to external liquid. It should be noted here that light can also pass through the split between the coreless fibers (as indicated by the red arrow below the SHF in Fig. 1). This situation is not discussed in the rest of the paper, because it is of the same condition as the lightpath inside the SHF.

The interference of the two interferometers can be represented by Eqs. 1 and 2, where $I_{h-opened}$, I_{silica} and $I_{h-closed}$ are the intensities of the light in the sensing arm, the silica part, and the reference arm, respectively. Additionally, $\phi_{sensing}$ and $\phi_{reference}$ are the phase differences of the two interferometers after the beams go through the sensing arm and the reference arm, respectively. They are expressed by Eqs. 3 and 4, where L_{SHF} is the length of the SHF, λ is the wavelength of the input light, and n^{eff}_{silica}, n^{eff}_{sample} and $n^{eff}_{reference}$ are the effective refractive indices of the modes in the silica glass, the sensing and the reference arm, respectively. Here, Δn_s (or Δn_r) is the effective RI difference between the modes in the silica glass and in the sensing (or reference) arm.

$$I_1 = I_{h-opened} + I_{silica} + 2\sqrt{I_{h-opened} I_{silica}}\cos\phi_{sensing} \tag{1}$$

$$I_2 = I_{h-closed} + I_{silica} + 2\sqrt{I_{h-closed} I_{silica}}\cos\phi_{reference} \tag{2}$$

$$\phi_{sensing} = \frac{2\pi}{\lambda}\left(n^{eff}_{silica} - n^{eff}_{sample}\right) L_{SHF} = \frac{2\pi \Delta n_s L_{SHF}}{\lambda} \tag{3}$$

$$\phi_{reference} = \frac{2\pi}{\lambda}\left(n^{eff}_{silica} - n^{eff}_{reference}\right) L_{SHF} = \frac{2\pi \Delta n_r L_{SHF}}{\lambda} \tag{4}$$

Therefore, transmission dips in the two MZIs occur at the phase differences of (2k+1) π (here, k is integer), and the corresponding wavelengths can be written as

$$\lambda^s_{dip} = \frac{2}{2k+1}\Delta n_s L_{SHF} \tag{5}$$

$$\lambda^r_{dip} = \frac{2}{2k+1}\Delta n_r L_{SHF} \tag{6}$$

Then, the free spectrum range (FSR) of both transmission spectra can be expressed by

$$FSR_s = \frac{\lambda^2}{\Delta n_s L_{SHF}} \tag{7}$$

$$FSR_r = \frac{\lambda^2}{\Delta n_r L_{SHF}} \tag{8}$$

where FSR_s and FSR_r are the FSRs of the reference interferometer and the sensing interferometer, respectively.

If Δn_s and Δn_r are closed to each other but not equal, the Vernier effect would be facilitated [24], [25]. As a result, the transmission spectrum would have a series of additional periodic fringes

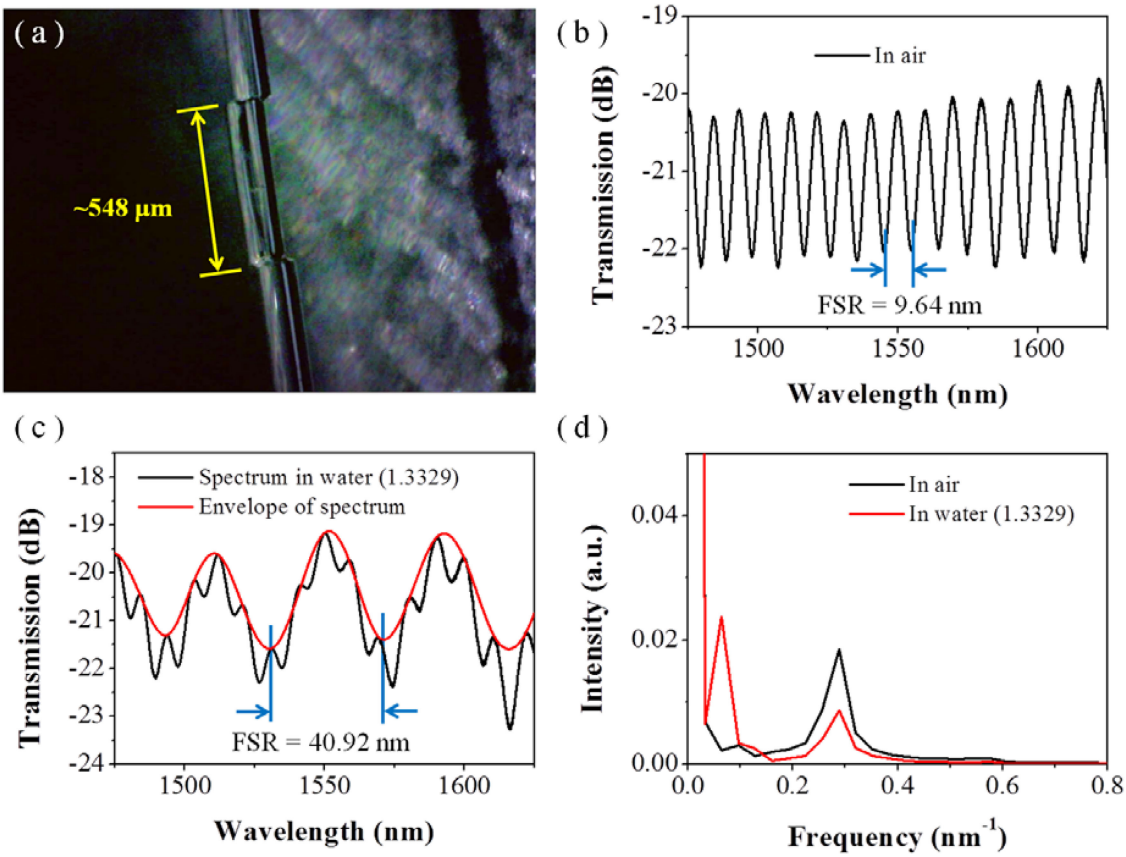

Fig. 2. Experimental results of the first sensor sample (S1), including the microscopic image (a), the transmission spectra in air (b) and water (c), and the calculated frequency spectra by fast Fourier transform (d).

with different amplitudes. The FSR of the transmission spectrum envelope $FSR_{envelope}$ can be described by

$$FSR_{envelope} = \left| \frac{FSR_s \times FSR_r}{FSR_s - FSR_r} \right| \tag{9}$$

Due to the Vernier effect, the envelope shift in response to the RI change is larger than the fringe shift in the original spectrum, which results in enhanced sensitivity.

In this paper, three types of sensors, namely S1, S2 and S3, are fabricated and explored. As a special feature of the structure, the SHF is laterally offset (S1 and S2) or side polished (S3) to expose one of its holes for liquid filling and to form two MZIs as well. The fabrication process of S1 and S2 start with the cleaving of a segment of lead-in SMF and a segment of CLF before they are spliced together by a fusion splicer (Fujikura 80C). Then, the spliced CLF part is cleaved again by a precision fiber cleaver to have a length of approximately 1 mm. Next, it is spliced to a segment of SHF using a polarization maintaining fiber fusion splicer (Fujikura FSM-100P+). Using the x-motor, the SHF is laterally offset from the optical axis by 30 to 35 μm in such a way that half the area of one of the two holes is covered by the CLF and the other half area remains open. During the fusion splicing of the SHF and the CLF, the discharge position is shifted to the CLF side by 30 μm, rather than at the middle of them. This action prevents the collapse of the holes of the SHF. After spicing, the SHF is shortened to approximately 500 μm long for S1 or 300 μm long for S2, and it is then spliced again with another section of CLF and SMF. The lengths of each of the fiber sections are examined by an optical microscope (Dino-Lite, AM7915MZT). In our tests, L_{SHF} of S1 is ~548 μm

as shown in Fig. 2(a), and L_{SHF} of S2 is ~351 μm, as shown in Fig. 6(a). As an improvement to the structure, the fabrication process of S3 is similar to the previous two sensors, and the specific details will be mentioned in the corresponding section later.

The fiber structure is numerically analyzed using the model analysis function in the wave optics module of COMSOL Multiphysics 5.3b software. The parameters of the SHF during the simulation are as follows: RIs are 1.452, 1.444 and 1.3329 for the core, the cladding, and the liquid in the hole, respectively; the diameters are 9 μm, 37 μm and 114 μm for the core, the air holes and the cladding, respectively. Two holes sit on both sides of the core with a gap (edge distance) of 12 μm.

For the RI sensing analysis, glucose-based solutions are used, and their RI values (n_D) are measured to the fourth digit using a digital refractometer. A linear relationship is also fit as follows:

$$\begin{cases} n = 1.14435 \times 10^{-4} \times a + 1.33288 \\ R^2 = 0.99959 \end{cases} \tag{10}$$

where a and n are the concentration (unit: mg/mL) and the RI of the glucose solution, respectively.

3. Results and Discussion

Fig. 2(a) presents the microscopic image of the first sensor sample (S1). Fig. 2(b) and 2(c) show the transmission spectra measured in air and in water, respectively. When S1 is in air, both the opened and closed holes are filled with the same material (i.e., air), Δn_s and Δn_r are identical, and thus, the spectrum resulted from the interference of the two identical MZIs. The FSR is found to be 9.64 nm. When one of the holes is filled with water ($n_D = 1.3329$ RIU), it caused a large difference between Δn_s and Δn_r. The black line in Fig. 2(c) plots the spectrum acquired in water, which shows additional periodic oscillations. The red line in Fig. 2(c) represents the envelope of this spectrum. The FSR of the envelope was 40.92 nm. To investigate the number and the power distribution of the modes, the interference spectra in air and water are transformed to the frequency domain by fast Fourier transform (FFT). The results are plotted in Fig. 2(d), which shows the changes of interference modes and intensities. For the sensor in air, there are two modes. When in water, the second mode is weakened, and an additional mode appears between the two previous modes. For the interference power, it is mainly distributed in the air hole (except for the core mode) when both the holes are filled with air. In contrast, the power in air is reduced by half when one hole is filled with water, and some power is transferred to the liquid. This finding shows that there are three modes in the structure when one hole is filled with liquid, i.e., the core mode, the mode in the air and the mode in the liquid. If we put these three RIs (~1, ~1.333 and ~1.45) of these three materials into Eq. 7 and Eq. 8, the values of FSR_s and FSR_r are close to 40.92 nm and 9.64 nm, respectively.

Fig. 3 shows the simulated distributions of the electric fields of the three modes for the wavelength of 1.55 μm at different polarizations. As marked with red characters and red arrows, the simulated distributions of the electric field on the left are based on vertical polarization, while the right shows the case of horizontal polarization. The effective mode indices of the three modes at different polarizations are also shown in Fig. 3. In the cases of both horizontal polarization and vertical polarization, the effective mode indices of the three modes are close to the RI of the corresponding three materials. Weighted averaging is performed according to the amplitudes of the electric field of the same mode in two polarizations to obtain the final effective mode index of the corresponding mode. For example, the final effective mode index of the core mode is determined to be 1.4487578. Next, we inserted these final effective RIs of three modes into Eqs. 1–4 and obtained the calculated spectrum as shown in Fig. 4. By comparing Fig. 4 and Fig. 2(c), it can be seen that these two spectra are very similar. The major difference lies in the values of the FSRs (38.73 nm in the calculation versus 40.92 nm in the experiment), which may be caused by the difference between the real RI and the RI assumed for the simulations, as well as the inaccurate measurement of the length of the SHF.

Next, the RI sensitivity of the sensor is investigated. Fig. 5(a) and (c) plot the envelopes of simulated and experimental spectra for the sample S1 when one of the holes has different

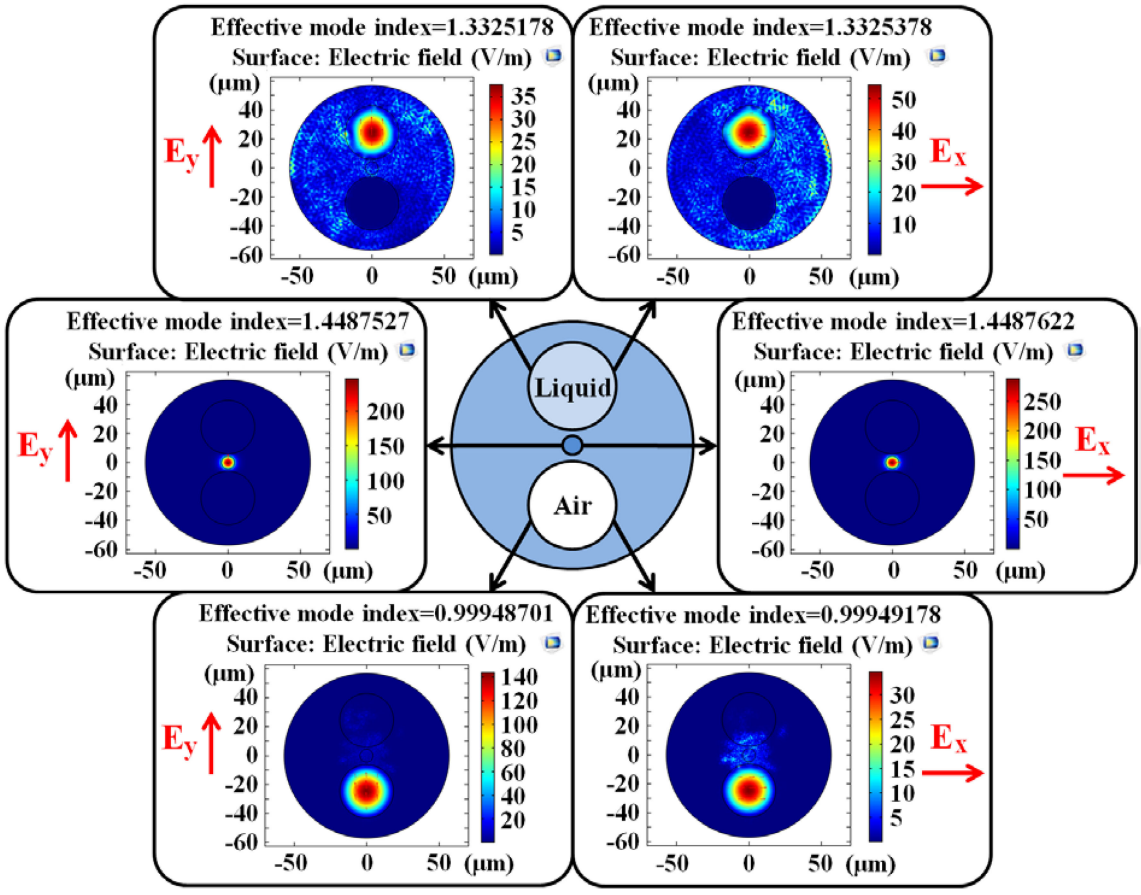

Fig. 3. Simulated field patterns of the side-hole fiber (SHF) when one of the holes is filled with water.

RIs. In the biosensing field where ultra-high sensitivity sensors are urgently needed to achieve sub-molecular-level detection, the refractive index of the sample to be tested is almost equal to that of water, so the refractive index range around 1.333 is firstly verified here. It can be seen that both envelopes of spectra exhibit a blue shift with an increase in RI. To estimate the sensitivity, the relationships between the wavelength shifts and the RI are plotted in Fig. 5(b) and 5(d) for the simulation and the experiment, respectively. Linear fits give the sensitivities at the level of 14,000 nm/RIU in both cases. It is noted that both have $R^2 > 0.999$, which proves the excellent linearity between the peak shift and the RI change.

The above RI sensitivity is quite high. However, it does not use the Vernier effect effectively. In the above experiment, one hole is filled with air and the other is filled with liquid, the difference between these two FSRs is very large ($FSR_s = \sim 40$ nm versus $FSR_r = \sim 10$ nm). In fact, the spectral envelope is merely the interference spectrum of only the sensing MZI, rather than the combination of the sensing MZI and the reference MZI. Moreover, the FSR is so small that the detectable RI range is greatly limited. The following discussion is based on these aspects.

To examine the influence of the SHF length, the second sensor sample S2 is fabricated with $L_{SHF} = \sim 350\,\mu$m. Fig. 6(a) presents the device photo, and Fig. 6(b) plots its spectrum and the envelope when the device is placed in water. The response is similar to that of the sample S1 in Fig. 2(c), but here it has FSR = 66.84 nm. The change in the FSR for both the sensors agrees well with Eq. 7, i.e., the FSR is inversely proportional to L_{SHF}. Similar to what is done in S1, the RI sensitivity of S2 is also investigated, as shown in Fig. 7. The value of the sensitivity of S2 is slightly lower than those of S1. Although L_{SHF} is shortened by ~30%, there is no significant change in the

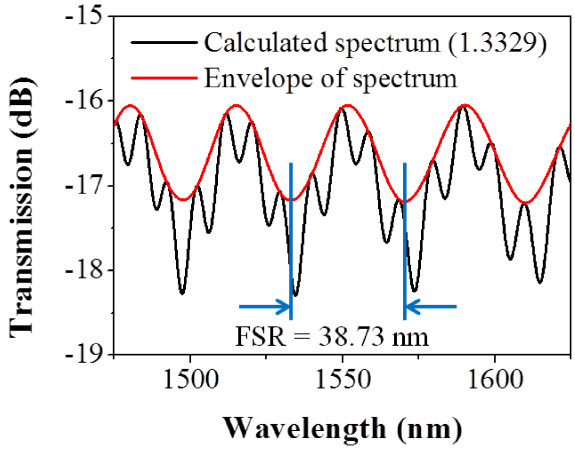

Fig. 4. Calculated spectrum (black line) and its envelope (red line) for the fiber sensor sample S1.

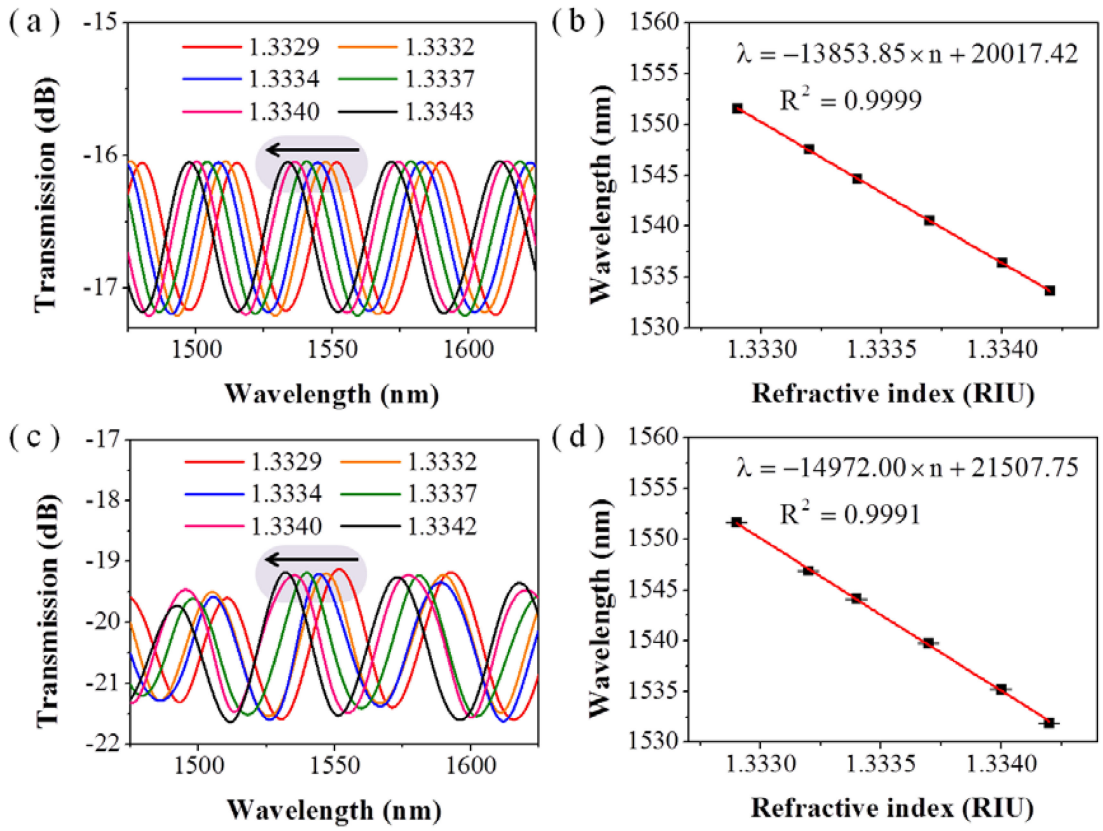

Fig. 5. Envelopes of the calculated (a) and the measured transmission spectra (c) for the sample S1 when one of SHF holes is filled with the liquids of varying RIs. Wavelength shift of the chosen peak is plotted and fit with respect to the RI for the calculated (b) and experimental results (d).

RI sensitivity. In addition, the decrease in L_{SHF} not only extends the detectable RI range due to the enlarged FSR but also reduces the required volume of liquid solution, which is calculated to be as low as 0.4 nL when one hole in this SHF section is fully filled. In brief, a shorter SHF does not affect the sensitivity but extends the RI detection range and reduces the required liquid sample volume.

As mentioned above, the Vernier effect does not play its role in samples S1 nor S2 because of the large difference between FSR_s (~40 nm) and FSR_f (~10 nm). To enable the Vernier effect, the

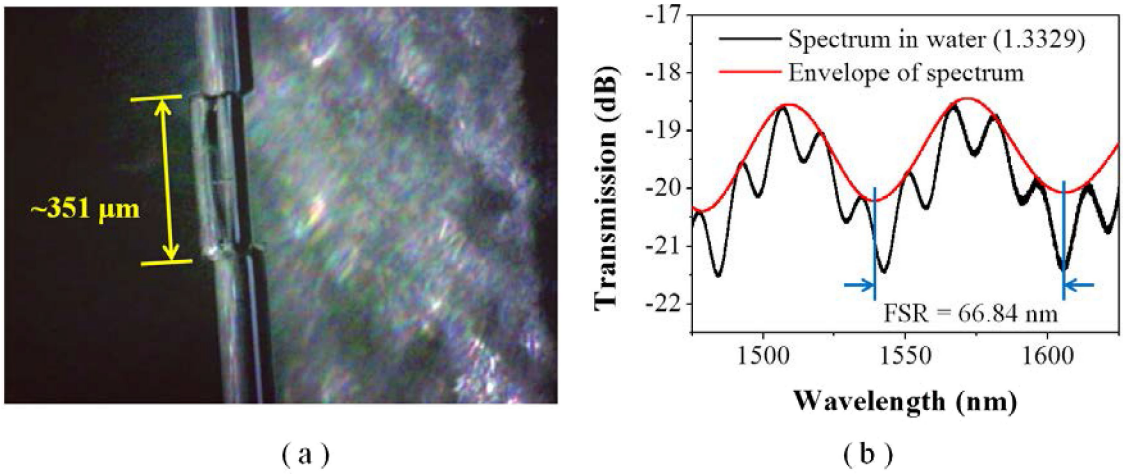

Fig. 6. (a) A microscope image of the sample S2 and (b) its spectrum (black line) together with the spectral envelope (red line) for measurements in water.

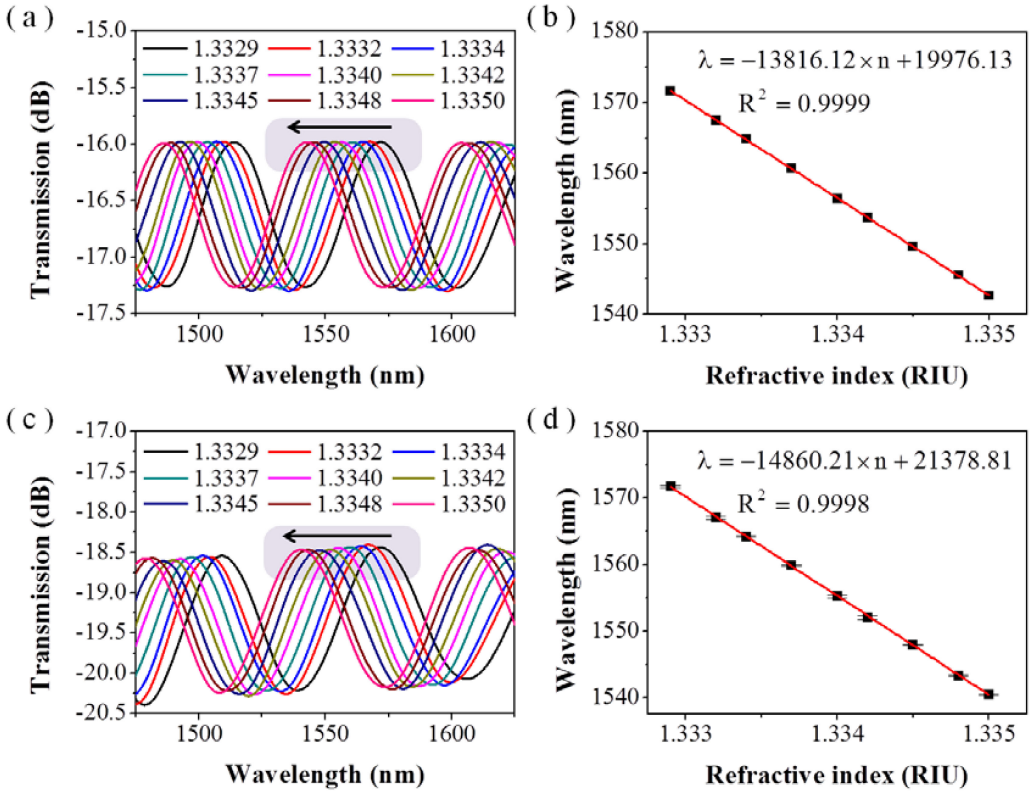

Fig. 7. Envelopes of the calculated (a) and the measured transmission spectra (c) for the sample S2 when one of SHF holes is filled with the liquids of varying RIs. Wavelength shift of the chosen peak is plotted and fit with respect to the RI for the calculated (b) and experimental results (d).

closed hole can be pre-filled with the liquid before the splicing, and therefore, $n^{eff}_{reference}$ becomes close to n^{eff}_{sample}, and in turn, FSR_r is close to FSR_s. In the experiment, another sensor sample S3 is fabricated (see Fig. 8). The liquid is mixed with red ink and filled into the holes of the SHF by capillary force. The red ink is to visualize the holes. Then, the SHF was side polished to open one of the holes. Next, a section of side polished SHF is fusion spliced between the sections of CLF and

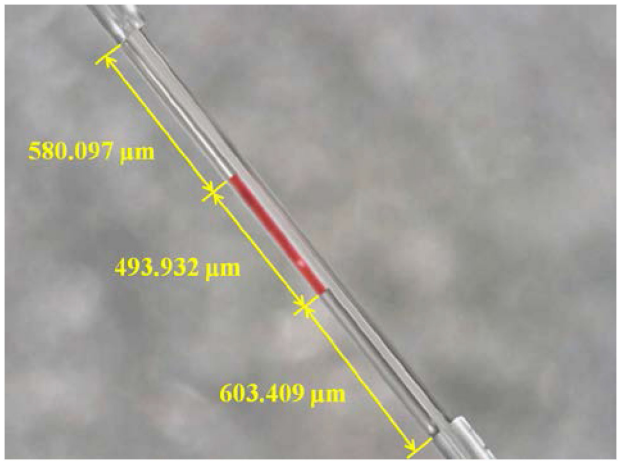

Fig. 8. Microscopic image of the sample S3.

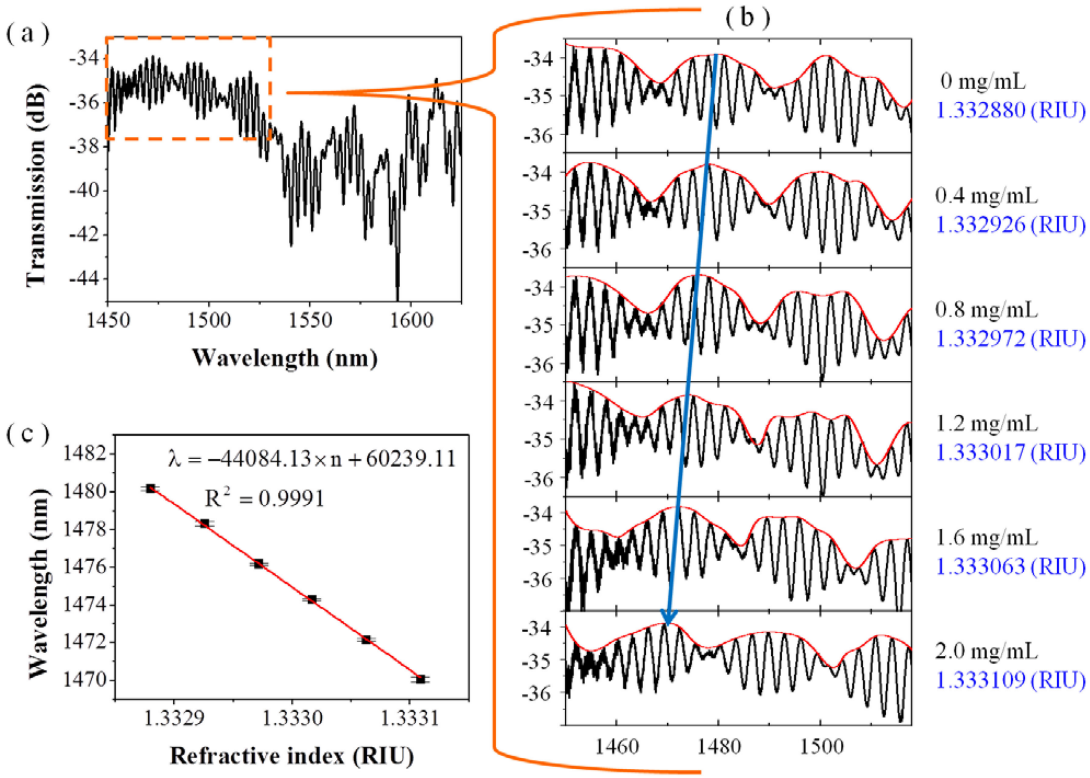

Fig. 9. (a) Transmission spectrum of the sample S3 in the glucose solution. (b) The selected spectral part (black line) and its envelope (red line) of S3 in different glucose solutions with different concentrations. (c) Wavelength shift of the chosen peak versus the RI.

SMF. It should be noted that there is no need for lateral offset because one of the holes is already opened. In S3, the length of the filled section is approx. 500 μm. There are 580 μm and 600 μm long empty regions on both sides of the red region, which is due to the evaporation of the liquid at high temperatures during the splicing stage. The RI of the mixture is $n_D = 1.3626$ RIU.

The spectral response for the sample S3 is shown in Fig. 9(a). The overall transmission is lower compared with the other non-polished sensors, which is mainly due to the increased length of the

TABLE 1
The Performance Comparison of Above Sensors

Sensor	Feature	FSR (nm)	Sensitivity (nm/RIU)	RI sensing range (RIU)	LOD (RIU)
S1	L_{SHF} = ~550 μm	40.92	14,972.00	2.73×10^{-3}	1.9×10^{-5}
S2	L_{SHF} = ~350 μm	66.84	14,860.21	4.50×10^{-3}	2.2×10^{-5}
S3	Vernier effect	25	44,084.13	5.67×10^{-4}	9.5×10^{-6}

light propagation in the liquid and the large absorption of the mixture in the reference arm. In the short wavelength range of the spectrum, the envelope is found to characterize the Vernier effect. The distortion occurs in the long wavelength range may be because the liquid is not fully filling the reference arm. Moreover, the mixture might not be uniformly distributed in the hole and could even contain some micro-bubbles.

Next, sensor S3 is immersed into glucose solutions of different concentrations (0 mg/mL, 0.4 mg/mL, 0.8 mg/mL, 1.2 mg/mL, 1.6 mg/mL and 2 mg/mL), and it captures the spectra as plotted in Fig. 9(b). The RIs of the glucose ranged from 1.33288 to 1.33311 RIU according to Eq. 10. Fig. 9(c) plots and linearly fits the wavelength shift of the chosen peak with respect to the RI of the glucose solution. The RI sensitivity reaches over 44,000 nm/RIU, which corresponds to a limit of detection (LOD) at the level of 1.0×10^{-5} RIU. Compared with samples S1 and S2, sample S3 improved the sensitivity by ~3 times thanks to the Vernier effect. If the reference arm is fully filled with the liquid, then the improvement factor would be larger, and the shape of the spectrum will be more unified. To clearly show the sensing performance of these three sensors, the relevant data is listed in Table 1.

In addition to the biosensing field with low refractive index, there may be occasions where it is desirable to detect samples with higher refractive indices [26]. We have configured samples with different refractive index ranges and different sample types to illustrate the detection performance and universality of our device. The samples used here included NaCl solution with refractive index of 1.3553~1.3576, sucrose solution with refractive index of 1.3872~1.3893, and glycerin solution with refractive index close to the cladding of fiber and even higher than cladding (1.4285~1.4300, 1.4665). Figs. 10(a)–10(d) show the experimental spectrum (black line) and its envelope (red line) for the fiber sensor sample S1 in NaCl solution with refractive index of 1.3570, sucrose solution with refractive index of 1.3879 and glycerine with refractive index of 1.4298 and 1.4665. In these different types of solutions with different refractive index, the spectra still remain the same characteristic as the spectrum in the previous solution with low refractive index does, i.e., a large period oscillation overlap with a small period oscillation. It demonstrates that the formulas given and the method used in our proposed approach apply to fluids with a diverse refractive index range, even if the refractive index is close to that of the cladding of fiber, or higher. However, we can also noticed that as the refractive index of the sample increases, the refractive index difference between the core and the liquid decreases, and the FSR becomes larger, which is consistent with Eq. 7. It can be seen from Fig. 10(d) that for the case of a refractive index of 1.4665, the FSR is already larger than the spectral range we used, which causes great trouble for refractive index sensing. Therefore, the samples used in our next refractive index test only include the first three cases.

NaCl solution with RI of 1.3553~1.3576, sucrose solution with RI of 1.3872~1.3893 and glycerine with RI of 1.4285~1.4300 were used to test the sensitivity of fiber sensor sample S1. As the same with previous solution with low refractive index, the envelopes of these spectra also exhibit a blue shift with an increase in RI, which is not given in this paper to avoid being verbose. Figs. 11(a)–11(c) show the linear fitting results of the relationship curves between the shift envelopes and the refractive index of sample in the range of 1.3553~1.3576, 1.3872~1.3893 and 1.4285 ~1.4300,

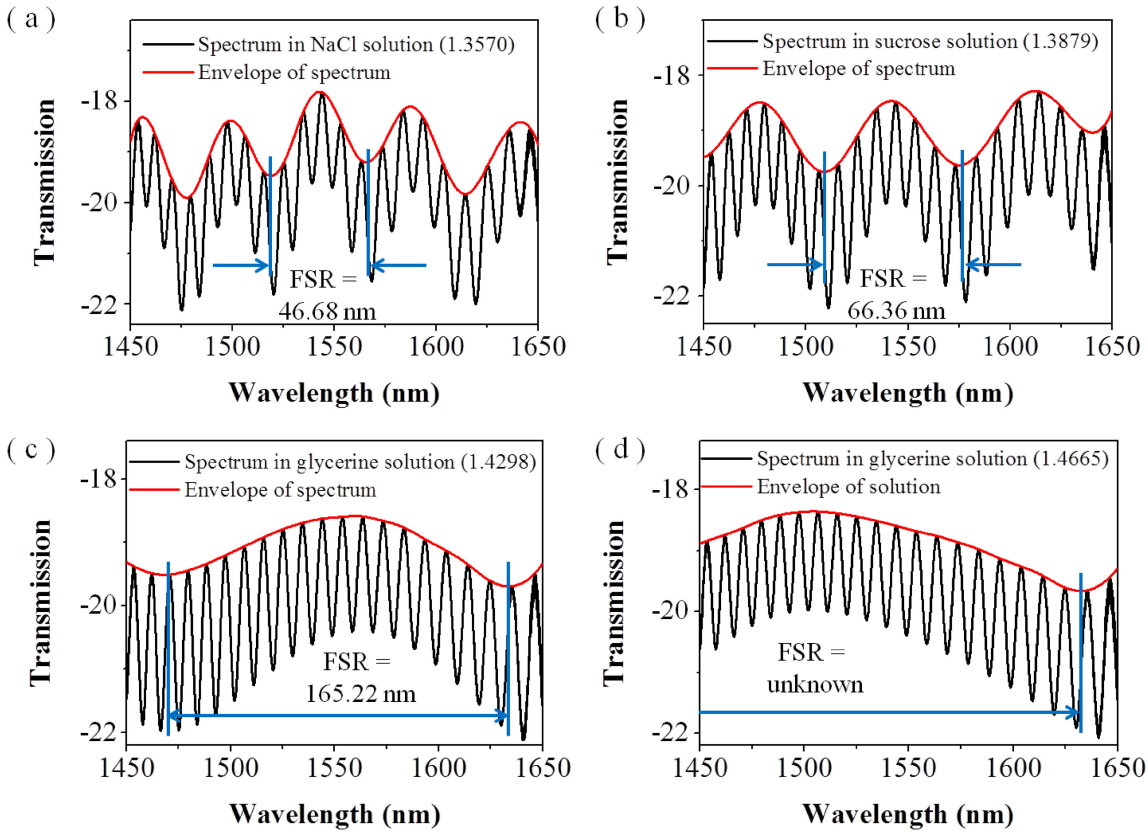

Fig. 10. Experimental spectrum (black line) and its envelope (red line) for the fiber sensor sample S1 in (a) NaCl solution with refractive index of 1.3570, (b) sucrose solution with refractive index of 1.3879 and glycerine with refractive index of (c) 1.4298 and (d) 1.4665.

respectively. The overview of sensitivity over different refractive index ranges and fitting of sensitivity changes with refractive index increases were also shown in Fig. 11(d). As the refractive index of liquid increases, the sensitivity rises exponentially. The corresponding fitting formula is shown as follows:

$$\begin{cases} S = 2.16113 \times 10^{-19} \times e^{n/0.02657} + 13409.55225 \\ R^2 = 0.9986 \end{cases} \tag{11}$$

where S is the sensitivity. In the vicinity of the refractive index of 1.334, the sensing sensitivity of fiber sensor sample S1 is 14972.00 nm/RIU as described above. When the refractive index increases to around 1.356, 1.388 and 1.429, the sensing sensitivity is 15530.58, 24929.90 and 62586.61 nm/RIU, respectively. This is because according to the formula (5),

$$\begin{cases} \lambda_1 = \frac{2}{2k+1} \Delta n_1 L_{SHF} \\ \lambda_2 = \frac{2}{2k+1} \Delta n_2 L_{SHF} \end{cases} \Rightarrow S = \frac{\lambda_1 - \lambda_2}{n_1 - n_2} = \frac{\lambda_1 - \lambda_2}{\triangle n_1 - \triangle n_2} = \frac{2}{2k+1} L_{SHF} \tag{12}$$

the sensitivity is inversely proportional to k. For the purpose of measurement, this λ must be within a specific range, when the refractive index of the sample increases, Δn as well as k decreases, thus the sensitivity also increases. What's more, as the refractive index of the sample approaches the refractive index of the fiber, the influence of this change increases dramatically, resulting in a significant promotion in the rate of sensitivity improvement.

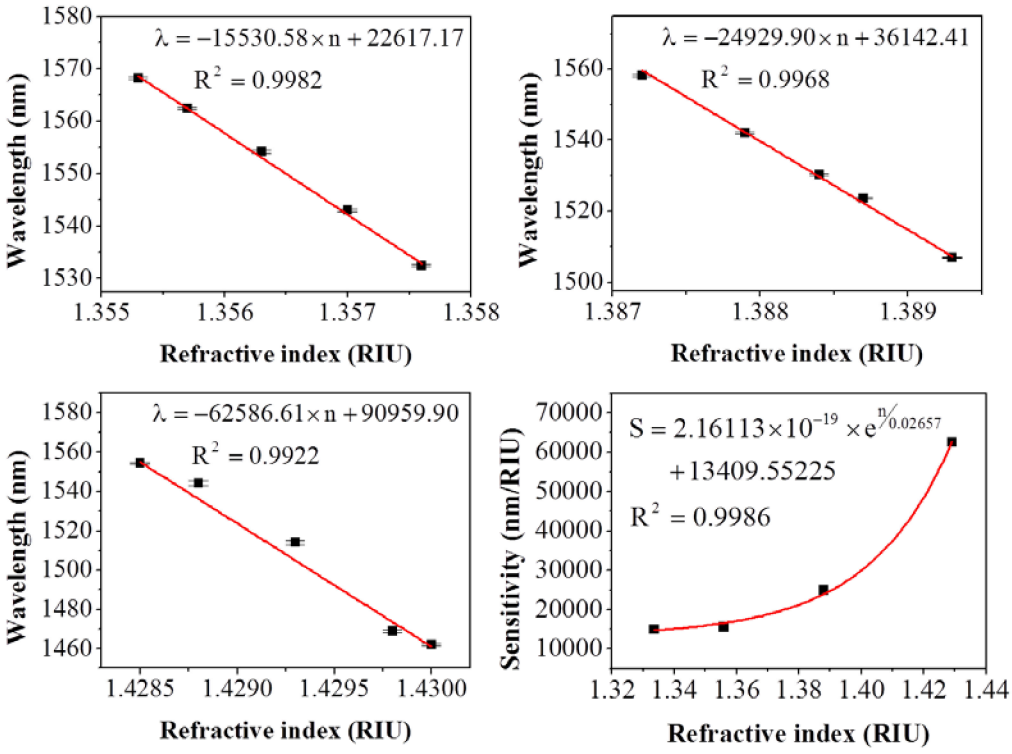

Fig. 11. Linear fitting results of the relationship curves between the shift envelopes of fiber sensor sample S1 and the refractive index of sample in the range of (a) 1.3553∼1.3576, (b) 1.3872∼1.3893, (c) 1.4285∼1.4300 and (d) overview of sensitivity over different refractive index ranges and fitting of sensitivity changes with refractive index increase.

Fig. 12. Simple packaging of the sensor.

Finally, to ensure the mechanical stability of the sensors, simple packaging protection was developed. We heat and melt both ends of the heat-shrinkable tube to wrap the fiber microstructure, and used a syringe to inject and discharge the liquid samples. Fig. 12 exemplifies a packaged device.

4. Conclusion

A unique type of refractive index sensor is proposed and studied by splicing a short section of side-hole fiber (SHF) with two coreless fibers (CLFs) and two single-mode fibers (SMFs). The SHF is laterally offset to expose one of its two holes to the external liquid. On the input side, the SMF leads in the light and the CLF expands the beam size, enabling us to feed light into the two holes and the silica part of the SHF. Each hole and the silica part form a Mach-Zehnder interferometer (MZI), and therefore, this sensor has dual MZIs. Experimental studies and theoretical calculations show that the sensitivity reaches 14,000 nm/RIU when the closed hole is filled with air and the open

hole is filled with liquid, and the SHF section length has little influence on the sensitivity. When the closed hole is pre-filled with liquid to facilitate the Vernier effect, the sensitivity is enhanced by a factor of 3.1 to 44,000 nm/RIU, which corresponds to the limit of detection (LOD) down to the level of 1×10^{-5} RIU. This sensor could find potential applications that require highly-sensitive refractive index measurements at points of interest, such as label-free biosensing, chemical analyses and medical diagnoses.

References

[1] S. Bandyopadhyay, T. K. Dey, and N. Basumallick, "High sensitive refractometric sensor using symmetric cladding modes of an FBG operating at mode transition," *J. Lightw. Technol.*, vol. 34, no. 14, pp. 3348–3353, Jul. 2016.

[2] T. Wang, K. Liu, and J. Jiang, "Temperature-insensitive refractive index sensor based on tilted moiré FBG with high resolution," *Opt. Exp.*, vol. 25, no. 13, 2017, Art. no. 14900.

[3] M. Śmietana, M. Koba, and P. Mikulic, "Towards refractive index sensitivity of long-period gratings at level of tens of μm per refractive index unit: Fiber cladding etching and nano-coating deposition," *Opt. Exp.*, vol. 24, no. 11, pp. 11897–11904, 2016.

[4] H. Li and P. Wang, "Helical long-period grating formed in a thinned fiber and its application to a refractometric sensor," *Appl. Opt.*, vol. 55, no. 6, pp. 1430–1434, 2016.

[5] D. Wu, T. Zhu, M. Deng, D. W. Duan, and L. L. Shi, "Refractive index sensing based on Mach–Zehnder interferometer formed by three cascaded single mode fiber tapers," *Appl. Opt.*, vol. 50, no. 11, 2011, Art. no. 1548.

[6] C. R. Biazoli, S. Silva, M. A. Franco, O. Frazão, and C. Cordeiro, "Multimode interference tapered fiber refractive index sensors," *Appl. Opt.*, vol. 51, pp. 5941–5945, 2012.

[7] W. B. Ji, H. H. Liu, and S. C. Tjin, "Ultrahigh sensitivity refractive index sensor based on optical microfiber," *IEEE Photon. Technol. Lett.*, vol. 24, no. 20, pp. 1872–1874, Oct. 2012.

[8] P. Wang, G. Brambilla, and M. Ding, "Enhanced refractometer based on periodically tapered small core singlemode fiber," *IEEE Sensors J.*, vol. 13, no. 1, pp. 180–185, Jan. 2013.

[9] R. Różycki-Bakon, M. Koba, and P. Firek, "Stack of nano-films on optical fiber end face for label-free bio-recognition," *J. Lightw. Technol.*, vol. 34, no. 23, pp. 5357–5362, Dec. 2016.

[10] X. Li, Y. Shao, and Y. Yuan, "A highly sensitive fiber-optic Fabry–Perot interferometer based on internal reflection mirrors for refractive index measurement," *Sensors*, nol. 16, no. 6, pp. 794–805, 2016.

[11] Z. Li *et al.*, "Ultrasensitive magnetic field sensor based on an in-fiber Mach–Zehnder interferometer with a magnetic fluid component," *Photon. Res.*, vol. 4, no. 5, pp. 197–201, 2016.

[12] W. Qi, L. Kong, and Y. Dang, "High sensitivity refractive index sensor based on splicing points tapered SMF-PCF-SMF structure Mach–Zehnder mode interferometer," *Sensors Actuators B, Chem.*, vol. 225, pp. 213–220, 2016.

[13] F. Ahmed, V. Ahsani, and L. Melo, "Miniaturized tapered photonic crystal fiber Mach–Zehnder interferometer for enhanced refractive index sensing," *IEEE Sensors J.*, vol. 16, no. 24, pp. 8761–8766, May 2016.

[14] Y. Zhao, F. Xia, and H. F. Hu, "A novel photonic crystal fiber Mach–Zehnder interferometer for enhancing refractive index measurement sensitivity," *Opt. Commun.*, vol. 402, pp. 368–374, 2017.

[15] Y. Zhao, A. Zhou, and H. Guo, "An integrated fiber Michelson interferometer based on twin-core and side-hole fibers for multi-parameter sensing," *J. Lightw. Technol.*, vol. 36, no. 4, pp. 993–997, Feb. 2017.

[16] S. M. A. Musa, N. F. Baharin, and A. I. Azmi, "Double-clad fiber Michelson interferometer for measurement of temperature and refractive index," *Microw. Opt. Technol. Lett.*, vol. 60, no. 4, pp. 822–827, 2018.

[17] Y. Wang and M. Yang, "Fiber in-line Mach–Zehnder interferometer fabricated by femtosecond laser micromachining for refractive index measurement with high sensitivity," *J. Opt. Soc. Amer. B*, vol. 27, no. 3, pp. 370–374, 2010.

[18] Z. Li *et al.*, "Label-free detection of bovine serum albumin based on an in-fiber Mach–Zehnder interferometric biosensor," *Opt. Exp.*, vol. 25, no. 15, pp. 17105–17113, 2017.

[19] B. Li *et al.*, "Sensitive real-time monitoring of refractive indices and components using a microstructure optical fiber microfluidic sensor," *Opt. Lett.*, vol. 43, no. 20, pp. 5070–5073, 2018.

[20] Z. Liu, H. Tam, L. Htein, M. V. Tse, and C. Lu, "Microstructured optical fiber sensors," *J. Lightw. Technol.*, vol. 35, no. 16, pp. 3425–3439, Aug. 2017.

[21] J. Yuan, Z. Kang, F. Li, G. Zhou, H. Y. Tam, and P. K. A. Wai, "Polarization-dependent intermodal four-wave mixing in a birefringent multimode photonic crystal fiber," *Opt. Lett.*, vol. 42, pp. 1644–1647, 2017.

[22] N. Luan, L. Zhao, and Y. Lian, "A high refractive index plasmonic sensor based on D-shaped photonic crystal fiber with laterally accessible hollow-core," *IEEE Photon. J.*, vol. 10, no. 5, Oct. 2018, Art. no. 6803707.

[23] H. Wang, X. Yan, and S. Li, "High sensitivity refractive index sensor based on dual-core photonic crystal fiber with hexagonal lattice," *Sensors*, vol. 16, no. 10, pp. 1655–1664, 2016.

[24] Y. Yang *et al.*, "Sensitivity-enhanced temperature sensor by hybrid cascaded configuration of a Sagnac loop and a F-P cavity," *Opt. Exp.*, vol. 25, no. 26, pp. 33290–33296, 2017.

[25] H. Lin, F. Liu, H. Guo, A. Zhou, and Y. Dai, "Ultra-highly sensitive gas pressure sensor based on dual side-hole fiber interferometers with Vernier effect," *Opt. Exp.*, vol. 26, no. 22, pp. 28763–28772, Oct. 2018.

[26] A. Basgumus, F. E. Durak, A. Altuncu, and G. Yilmaz, "A universal and stable all-fiber refractive index sensor system," *IEEE Photon. Technol. Lett.*, vol. 28, no. 2, pp. 171–174, Jan. 2016.